Research on Engineering Structures & Materials
www.jresm.org
Research Group

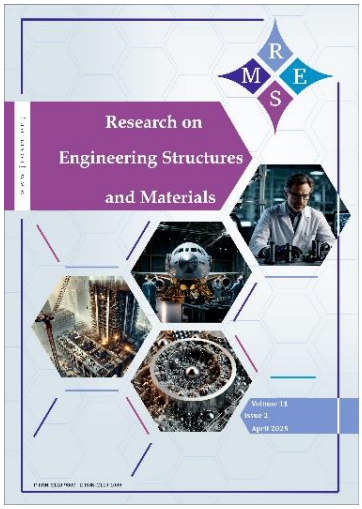

Adaptive multi-sensor fusion for pedestrian indoor positioning using UCR-DTW, improved CRF, and SAGE-HUSA filtering

Wei Gao, HaiPeng Yang

Online Publication Date: 30 August 2026

URL: http://www.jresm.org/archive/resm2026-1873vk0714rs.html
DOI: http://dx.doi.org/10.17515/resm2026-1873vk0714rs

Journal Abbreviation: *Res. Eng. Struct. Mater.*

To cite this article
Gao W, Yang H. Adaptive multi-sensor fusion for pedestrian indoor positioning using UCR-DTW, improved CRF, and SAGE-HUSA filtering. *Res. Eng. Struct. Mater.*, 2026; 12(5): 3719-3736.

Disclaimer
All the opinions and statements expressed in the papers are on the responsibility of author(s) and are not to be regarded as those of the journal of Research on Engineering Structures and Materials (RESM) organization or related parties. The publishers make no warranty, explicit or implied, or make any representation with respect to the contents of any article will be complete or accurate or up to date. The accuracy of any instructions, equations, or other information should be independently verified. The publisher and related parties shall not be liable for any loss, actions, claims, proceedings, demand or costs or damages whatsoever or howsoever caused arising directly or indirectly in connection with use of the information given in the journal or related means.

Published articles are freely available to users under the terms of Creative Commons Attribution - NonCommercial 4.0 International Public License, as currently displayed at here (the "CC BY - NC").

Research on Engineering Structures & Materials
www.jresm.org
MIM Research Group

Research Article

Adaptive multi-sensor fusion for pedestrian indoor positioning using UCR-DTW, improved CRF, and SAGE-HUSA filtering

Wei Gao [a], HaiPeng Yang [*,b]

Digital Media Department, HeBei Software Institute, Baoding, China

Article Info

Article History:

Received 14 July 2026

Accepted 25 Aug 2026

Keywords:

Indoor positioning;
Pedestrian dead reckoning;
Multi-sensor fusion;
Conditional random field;
UCR-DTW;
Sage-Husa filter;
Geomagnetic matching

Abstract

Indoor positioning in smart buildings is challenging because satellite signals are obstructed, while inertial navigation methods suffer from sensor noise, magnetic interference, and cumulative errors. This study proposes a high-precision indoor positioning method integrating Pedestrian Dead Reckoning (PDR), map matching, and multi-sensor fusion for real-time pedestrian positioning. The proposed framework employs acceleration and geomagnetic features for stationary state detection, Dynamic Time Warping (DTW) for adaptive gait recognition, and a robust adaptive Kalman filter for heading estimation. Building topology constraints are incorporated through an improved Conditional Random Field (CRF), which is combined with University of California Riverside-optimized DTW (UCR-DTW) for geomagnetic sequence matching. Finally, a Sage-Husa filter fuses multi-source information to generate robust position estimates. Experiments on the IPIN 2025 Competition Track 3 (Smartphone-based) indoor positioning dataset show that the proposed method achieves a mean positioning error of 0.45 m and a trajectory integrity rate of 98.2%. The improved CRF reaches a map-matching accuracy of 96.8% after six iterations and maintains 71.6% accuracy under level-5 magnetic interference. These results demonstrate that the proposed framework effectively suppresses cumulative errors and magnetic disturbances while constraining trajectories within navigable areas, providing accurate and reliable real-time positioning for pedestrian indoor navigation. Future work will incorporate height information during multi-storey transitions to further improve cross-floor positioning performance.

© 2026 MIM Research Group. All rights reserved.

1. Introduction

Smart buildings feature enclosed spaces with dense structural elements that significantly attenuate satellite signals. Indoor positioning faces significant challenges due to severe satellite signal attenuation and blockage [1]. For pedestrian indoor positioning applications, the indoor space has dense walls and complex layouts, and satellite signals are severely blocked, making it impossible to rely on traditional navigation and positioning. Current PDR systems exhibit cumulative drift, necessitating the integration of map matching techniques for constraint correction to achieve continuous and reliable positioning within intelligent buildings [2]. However, the proposed methodology faces significant limitations: the noise from consumer-grade sensors, the frequent switching of pedestrian motion states, and the magnetic interference from household appliances, metal furniture, etc. in the indoor environment lead to inaccurate gait detection, drift in course calculation, and rapid accumulation of errors along walking distance [3]. Meanwhile, existing positioning methods often lack sufficient topological constraints from indoor maps, so filtering-based correction alone cannot explicitly distinguish passable and impassable areas. Under high-

*Corresponding author: haipengy2@outlook.com
[a]orcid.org/0009-0009-2333-7179; [b]orcid.org/0009-0002-4230-4451
DOI: http://dx.doi.org/10.17515/resm2026-1873vk0714rs

noise inertial and geomagnetic measurements, particle-filter or standard Kalman-filter-based methods mainly suppress estimation noise but cannot reliably enforce wall, corridor, and obstacle constraints. As a result, accumulated positioning errors may still cause trajectories to cross walls or boundaries and deviate from the actual path. Existing map matching methods exhibit limitations in adaptive gait adjustment and robust heading estimation under magnetic interference. Furthermore, most existing fusion schemes lack a collaborative design that integrates noise adaptation, dynamic weight adjustment, and global path optimization, making it difficult to meet the requirements of long-term, high-precision stable operation and precise navigation of pedestrians in signal occlusion environments [4-5]. Therefore, the study first calculates the pedestrian trajectory in real time through PDR, uses multimode sensing to identify the motion state, and adaptively optimizes gait detection and course solution. The study then combines map matching calibration with the electronic map and applies spatial constraints using Conditional Random Fields (CRFs). The UCR Suite optimization techniques are integrated into the DTW algorithm to construct the UCR-DTW framework for rapid geomagnetic matching [6-7]. A positioning process that works in tandem with adaptive filtering and map correction is built. The study aims to address error accumulation, magnetic interference, and trajectory out-of-bounds to achieve sub-meter base station-free positioning and support pedestrian navigation and tracking.

The main innovations of this study are summarized as follows. First, in the PDR segment, acceleration and geomagnetic features are jointly used for stationary-state detection, reducing false step counting caused by slight body movement or sensor disturbance. A DTW-based adaptive gait detection model is then constructed to identify different walking states and dynamically adjust peak-detection parameters, while a robust adaptive Kalman filter under least-squares constraints is employed for heading estimation. Second, in the map-matching segment, an improved CRF model is developed by incorporating geomagnetic matching features and adaptive weight updating, thereby strengthening spatial constraints on candidate trajectories under varying measurement reliability. In addition, the UCR-DTW strategy is introduced to accelerate geomagnetic sequence matching, and these components are integrated into a PDR-geomagnetic-map-matching fusion positioning framework.

The remainder of this paper is organized as follows. Section 2 reviews related studies on indoor positioning and multi-source fusion. Section 3 presents the proposed methodology, including motion-state recognition and adaptive PDR parameter estimation, improved CRF-based map matching, and geomagnetic-assisted fusion positioning. Section 4 evaluates the positioning accuracy, real-time performance, convergence, robustness, and ablation results. Finally, Section 5 summarizes the main findings and discusses the limitations and future work.

2. Related Works

Indoor positioning studies can be broadly grouped according to the information source and constraint mechanism used for position estimation. Existing research mainly includes signal- or fingerprint-based positioning, inertial and motion-assisted positioning, and map-constrained fusion approaches. These directions provide complementary advantages, but their limitations in motion adaptation, interference resistance, and spatial constraint management remain important issues for continuous pedestrian positioning.

In signal- and fingerprint-based positioning, Han Y et al. developed a crowdsourcing positioning model to improve feature extraction and the utilization of unlabeled fingerprint data. Their approach introduced a spatial fingerprint attention encoder and a signal-strength masking mechanism, resulting in improved positioning accuracy over conventional algorithms [8]. Pinto B et al. proposed an access-point selection strategy based on least-squares estimation and Bluetooth Low Energy measurements. Their method reduced the positioning error by up to 13% compared with conventional least-squares estimation and by up to 30% compared with the k-nearest-neighbor method [9]. Nguyen D K et al. combined truncated singular value decomposition with a long short-term memory model to reduce the computational burden of Wi-Fi fingerprint positioning while maintaining positioning accuracy [10]. These methods improve the exploitation

of radio-frequency fingerprints, but their performance remains dependent on the stability and distinctiveness of environmental signal features.

For motion-assisted and inertial positioning, Yang Y et al. developed an algorithm combining Brownian-motion correction and dynamic parameter optimization. Their algorithm used prior motion information to correct positioning results and achieved a maximum average positioning error of 3.31 m [11]. Assayag Y et al. combined particle swarm optimization with a signal-propagation model to reduce the dependence on pre-training in indoor ranging, reporting an average positioning error of 2.57 m [12]. Such approaches improve position estimation by introducing motion priors or optimization mechanisms, but accumulated motion errors and sensor disturbances remain difficult to suppress over long trajectories. In particular, pedestrian dead reckoning requires reliable step detection, walking-state discrimination, and heading estimation, which motivates the use of adaptive motion-state recognition and filtering rather than fixed-parameter correction.

Map-constrained positioning provides another means of limiting accumulated trajectory drift. Xu Z et al. developed a mapping method combining an improved beetle swarm algorithm with an efficient matching strategy, which reduced computation time and particle resampling while improving mapping accuracy [13]. However, optimization- or particle-based mapping alone does not explicitly guarantee that the estimated trajectory satisfies indoor topological constraints such as walls, corridors, and obstacles. Under noisy inertial or geomagnetic observations, insufficient constraint management may still result in wall crossing, boundary violations, or deviation from feasible paths. Probabilistic state-sequence modelling is therefore required to jointly consider observation information and spatial connectivity. In this study, an improved CRF is introduced for this purpose, in which geomagnetic matching information is incorporated into the state feature function and the feature weights are adaptively updated according to data reliability.

The above studies also reveal a separation between signal matching, motion estimation, and map constraints. Signal-based approaches make effective use of environmental fingerprints but can be sensitive to local signal variations; inertial approaches provide continuous positioning but suffer from cumulative drift; and existing mapping or optimization approaches do not fully coordinate observation reliability with indoor topological constraints. Moreover, the cited studies involve different positioning targets, including crowdsourced pedestrian positioning and mobile-robot mapping.

Therefore, the remaining gaps are addressed through an integrated pedestrian-positioning framework. Acceleration and geomagnetic dual features are first used for stationary-state recognition, while DTW enables adaptive gait detection. UCR-DTW is then employed for efficient geomagnetic sequence matching, and the improved CRF introduces geomagnetic features and adaptive weights to impose indoor topological constraints. Finally, Sage-Husa adaptive filtering dynamically estimates measurement uncertainty and fuses PDR and geomagnetic observations. Through this combination, the proposed method targets both poor interference resistance and insufficient utilization of heterogeneous sensing and spatial information while reducing accumulated trajectory drift.

3. Methodologies and Materials

3.1 Motion State Recognition Based on Multi-Model Features and Adaptive PDR Parameter Estimation

Smart building spaces are enclosed and satellite signals are difficult to penetrate, relying on PDR positioning. However, PDR is susceptible to noise, state changes and magnetic interference, errors accumulate rapidly, and the lack of spatial constraints leads to wall-penetrating drift [14-15]. Classical PDR usually estimates pedestrian displacement through step detection, step-length estimation, and heading update, among which acceleration-based empirical models such as the Kim model and related step-length estimators provide an important basis for subsequent adaptive PDR methods [16-17]. Existing map matching is inadequate in terms of state recognition, gait adaptation, etc., and is difficult to meet the requirements of high-precision and stable positioning.

To accurately distinguish between pedestrian motion and non-motion states and reduce the impact of static miscounting steps on positioning, a non-motion state recognition method based on acceleration and geomagnetic standard deviation is studied to achieve stable state determination through two-dimensional features. The developed approach for identifying non-motion states based on acceleration and geomagnetic standard deviation is shown in Figure 1.

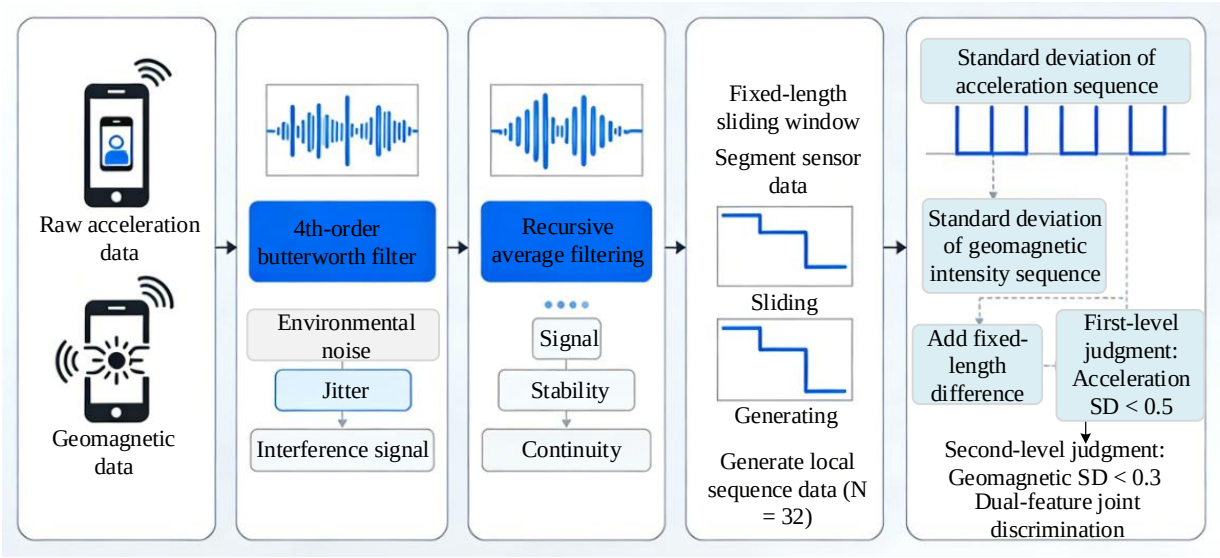

Fig. 1. Flow chart of non motion state recognition based on acceleration and geomagnetic standard deviation

According to Figure 1, the raw acceleration, gyroscope, and geomagnetic data collected by the smartphone were first synchronized according to their timestamps and uniformly resampled at 100 Hz. Subsequently, a fourth-order low-pass Butterworth filter with a cutoff frequency of 5 Hz was applied to suppress high-frequency noise and device vibration while preserving the dominant low-frequency components associated with gait and attitude changes. The data are subsequently smoothed using recursive average filtering to improve signal stability and continuity. A fixed-length sliding window is then used to segment the continuous sensor data and generate local sequences. Within each window, the standard deviations of the acceleration and geomagnetic intensity sequences are calculated, followed by the computation of feature differences between fixed-interval windows to characterize short-term variation trends. The acceleration features are then used for the first-level judgment, while the geomagnetic features are incorporated into the second-level judgment to achieve dual-feature joint recognition of motion states. In each sliding window, the standard deviation of the acceleration sequence and the standard deviation of the geomagnetic intensity sequence are calculated respectively, the standard deviation of the acceleration is shown in Equation (1).

$$\sigma_a = \sqrt{\frac{1}{N_a}\sum_{p=1}^{N_a}(a_p - \bar{a})^2} \tag{1}$$

In Equation (1), where N represents the total number of sampling points within the sliding window; a_p represents the acceleration amplitude of the sampled point p; $\bar{a}$ represents the mean of the acceleration sequence within the window. The standard deviation of geomagnetic intensity is as shown in Equation (2).

$$\sigma_m = \sqrt{\frac{1}{N_m}\sum_{q=1}^{N_m}(m_q - \bar{m})^2} \tag{2}$$

In Equation (2), where m_q represents the total geomagnetic intensity at the sampling point q; $\bar{m}$ represents the mean of the geomagnetic intensity within the window. This method uses the

acceleration standard deviation for the first-level state discrimination, with the threshold set to 0.5. When the acceleration feature alone cannot clearly distinguish the state, the geomagnetic standard deviation is further introduced for second-level discrimination, with a threshold of 0.3. The two thresholds were determined according to the statistical distributions shown in Figure 7. The acceleration standard deviations of the stationary and slightly wobbling states were below 0.5, whereas the geomagnetic standard deviations of the non-motion states were below 0.3 and those of the motion states were above 0.3. Because the acceleration distributions of general wobbling and walking partially overlap, geomagnetic information is used as the secondary criterion.

To enable gait detection to adapt to different walking speeds and improve the accuracy of step counting, a motion state classification and adaptive peak threshold detection method based on the DTW algorithm is proposed. The detection parameters are dynamically adjusted according to the motion state to achieve robust gait recognition in multiple scenarios. The DTW-based adaptive gait detection method for pedestrian motion state classification and adaptive peak detection threshold determination is shown in Figure 2.

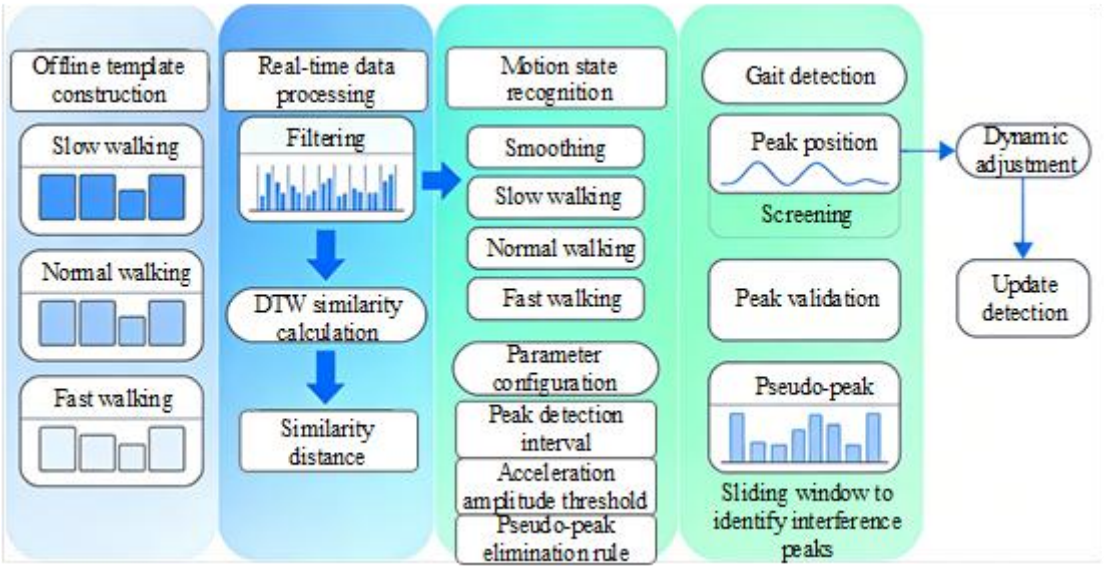

Fig. 2. Framework diagram of adaptive peak detection proposed methodology based on DTW

As shown in Figure 2, acceleration sequence templates corresponding to slow, normal, and fast walking were first constructed offline. For each motion state, 20 valid acceleration sequences were selected, with each sequence containing five consecutive complete gait cycles. After segmenting the sequences according to gait peaks, each individual gait cycle was uniformly resampled to 100 points using linear interpolation, and Z-score normalization was applied to reduce the influence of differences among individuals, device attitudes, and motion amplitudes. The normalized cycles belonging to the same motion state were then temporally aligned and averaged to obtain the three DTW reference templates. During online recognition, the real-time acceleration sequence was filtered and smoothed, and then processed using the same resampling and normalization procedures as those applied to the offline templates. The DTW algorithm was subsequently used to calculate the similarity distances between the real-time sequence and the three reference templates, and the current pedestrian walking state was determined according to the template with the minimum DTW distance. The DTW distance calculation is shown in Equation (3).

$$DTW(M,J) = min_{\pi} \sqrt{\sum_{(r,s)\in\pi} \|m_r - j_s\|^2} \tag{3}$$

In Equation (3), $DTW(M,J)$ represents the minimum distance between two time series calculated by the DTW algorithm; M represents the acceleration sequence collected in real time; J represents an offline template sequence; π represents a regular path from sequence M to sequence J; (r,s) represents a matching point pair on a regular path; $\|m_r - j_s\|$ represents the Euclidean distance

between points m_r and j_s. Based on the identified motion state, the system automatically configures the corresponding peak detection period threshold, acceleration amplitude threshold, and pseudo-peak elimination rule. During the gait detection phase, the processed acceleration signal is traversed point by point to search for the peak position, and effective peaks that conform to the walking pattern are screened based on the periodic constraint conditions, and false interference peaks are identified and eliminated through the sliding window. The algorithm continuously updates the detection parameters according to the changes in motion state, dynamically adjusts the constraints for peak recognition, and can perform adaptive gait detection and step count statistics in different motion modes.

To suppress the influence of indoor magnetic field anomalies on heading estimation, a robust adaptive Kalman filter under least-squares constraints is introduced. The method fuses the relative heading obtained from the gyroscope with the absolute heading estimated from the magnetometer and accelerometer, and adaptively updates the filtering parameters to obtain stable heading estimates, as shown in Figure 3.

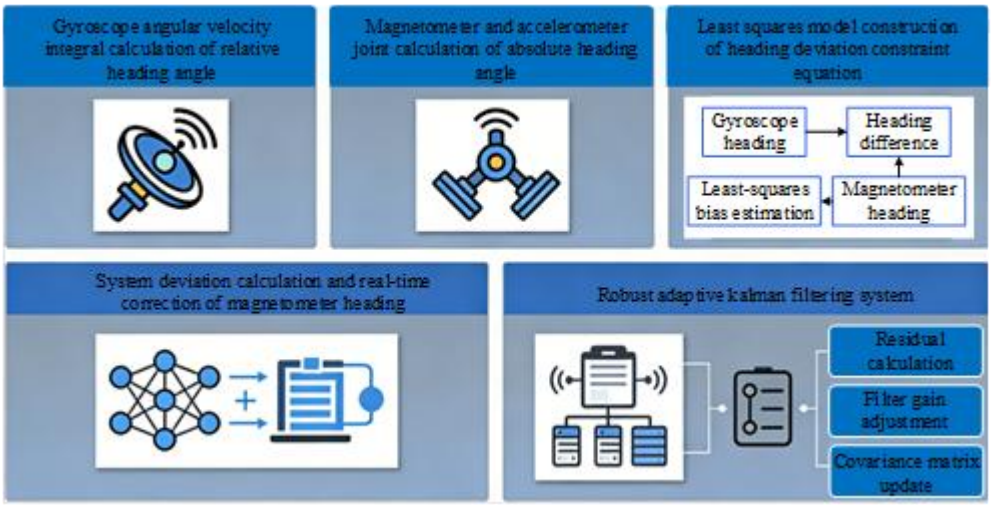

Fig. 3. Structure diagram of robust adaptive Kalman filter heading estimation

According to Figure 3, this method calculates the relative heading angle respectively by the gyroscope angular velocity product decomposition, and the absolute heading angle is calculated jointly by the magnetometer and the accelerometer. The gyroscope heading angle integral is shown in Equation (4).

$$\psi_{gyro}(t) = \psi_{gyro}(t-1) + \omega(t) \cdot \Delta t \tag{4}$$

In Equation (4), $\psi_{gyro}(t)$ represents the relative heading angle obtained by integrating the angular velocity of the gyroscope at current moment t; $t-1$ represents the previous moment; $\omega(t)$ indicates the angular velocity measured by the gyroscope at the current moment; Δt represents the time interval between two adjacent sampling moments. The magnetometer heading angle solution is as shown in Equation (5).

$$\psi_{mag} = arctan\left(\frac{K_y}{K_x}\right) \tag{5}$$

In Equation (5), ψ_{mag} represents the calculated absolute heading angle; K_y represents the magnetometer component in the y axial direction in the horizontal coordinate system; K_x represents the magnetometer component in the $x$axial direction in a horizontal coordinate system; $arctan$ represents the arctangent function. The study substitutes two sets of independently calculated heading angle data into the least squares model, constructs the heading deviation constraint equation, calculates the systematic deviation between the two sets of heading, and uses

this deviation to correct the heading angle output by the magnetometer in real time. The least squares heading deviation estimation $\hat{b}$ is as shown in Equation (6).

$$\hat{b} = (H^T H)^{-1} H^T (\psi_{gyro} - \psi_{mag}) \tag{6}$$

In Equation (6), H is the observation matrix describing the relationship between the systematic heading bias and the synchronized heading differences obtained from the gyroscope and magnetometer. For N synchronized samples, H has a dimension of $N \times 1$, and each element is equal to 1 because the same scalar heading bias is assumed to affect all observations. Therefore, each row of H maps the common heading bias to one heading-difference observation, and the least-squares solution estimates this systematic bias from all synchronized samples. H^T represents transposition of H; $(H^T H)^{-1}$ represent the inverse matrix of $H^T H$. The corrected heading data as observations and the gyroscope predicted heading as state predictions are both input into the anti-differential adaptive Kalman filtering system. During the filtering process, the residuals between the predicted values and the observed values are calculated in real time. The filtering gain and the observed noise weights are dynamically adjusted according to the residuals, while the system noise covariance matrix and the observed noise covariance matrix are continuously updated. The system performs recursive operations with the heading angle as the core state variable, continuously corrects the state estimation results, and completes a stable and reliable heading fusion solution.

3.2 Indoor Map Matching Proposed Methodology Based on Improved CRFs

After motion state recognition, adaptive gait detection and heading estimation, PDR positioning may still experience trajectory drift due to accumulated sensor errors, and phenomena such as wall penetration and boundary crossing are prone to occur in complex layouts of intelligent buildings [18-19]. To confine the positioning trajectory within a reasonable space, the study introduced indoor map constraints and proposed a CRF-based map matching method, using building topology and boundary information to correct the PDR results. The developed CRF-based map matching approach is shown in Figure 4.

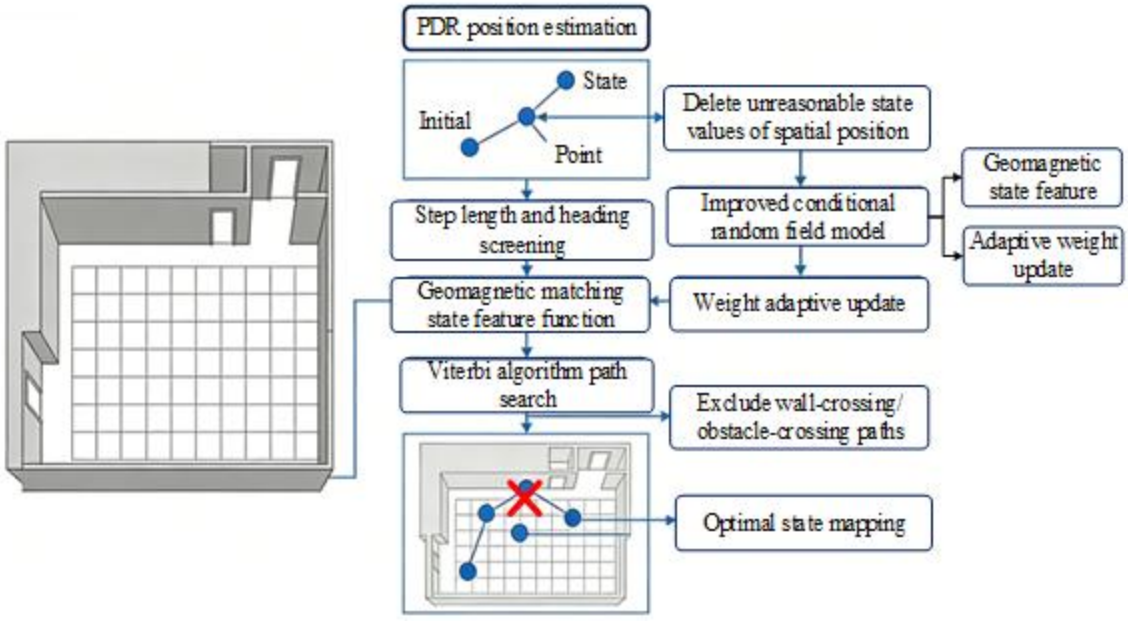

Fig. 4. Schematic diagram of map matching based on improved CRFs

According to Figure 4, the spatial boundary information of the indoor environment, including walls, corridors, corners, entrances, and exits, was first extracted. The indoor floor plan was then divided into uniform grid cells with a spatial resolution of 0.5 m × 0.5 m, and the walkable and non-walkable regions were labeled according to the building topology. This grid size provides sufficient spatial resolution for map constraints while limiting the number of CRF candidate states and avoiding the

substantial increase in computational complexity caused by excessively fine discretization. The initial candidate state points are generated based on the positions calculated by the PDR system. The candidate points are initially screened in combination with the step size information and heading information of the previous moment, and the state values with unreasonable spatial positions are deleted [20].

During candidate-state screening, the transition weights between adjacent CRF nodes are jointly determined by motion continuity and building-topology constraints. First, the feasibility of each state transition is evaluated according to the deviation between the Euclidean distance of adjacent candidate points and the PDR-estimated step length, as well as the deviation between the candidate transition direction and the current heading. Larger distance and heading deviations result in lower transition weights. Wall and obstacle information is then introduced as hard topological constraints in the edge-weight calculation. If the line segment connecting two candidate nodes crosses a wall, obstacle, or other non-walkable region, the corresponding transition is directly regarded as invalid and excluded from the subsequent Viterbi path search. For feasible transitions, the edge weights are assigned according to step-length consistency, heading consistency, and the confidence of geomagnetic matching. Through this mechanism, the CRF suppresses spatially unreasonable transitions at the state-transition stage and prevents wall-crossing, obstacle-crossing, and trajectories that significantly deviate from valid walkable regions during global path optimization. The screened valid state points are input into the CRFs model, and the geomagnetic matching results are used to construct the state feature function, and the feature function weights are adaptively updated based on the credibility of the data. The CRF state feature function is shown in Equation (7).

$$\Re(z_t, o_t) = exp\left(\sum_l \theta_l f_l(z_t, o_t)\right) \tag{7}$$

In Equation (7), $\Re(z_t, o_t)$ represents the potential function in the CRF; z_t represents the hidden state at moment$t$; o_t is the observation data at moment$t$; θ_l represents the weight of the lth feature function; f_l represents the lth feature function; exp represents the exponential function. In the improved CRF, geomagnetic matching results are introduced as an additional state feature to evaluate the consistency between each candidate position and the current geomagnetic observation. A higher geomagnetic matching similarity increases the preference for the corresponding candidate state. In addition, the contribution of the geomagnetic feature is adaptively adjusted according to the reliability of the observation data. Therefore, compared with a conventional CRF mainly based on spatial transition and observation constraints, the improved CRF further incorporates geomagnetic matching information and adaptive feature weighting into the state evaluation process. The Viterbi algorithm is used for global path search of the state sequence, and the Viterbi algorithm is recursively shown in Equation (8).

$$\delta_t(j) = max_i\left[\delta_{t-1}(i) \cdot \Psi(y_{t-1} = i, y_t = j, x_t)\right] \tag{8}$$

In Equation (8), $\delta_t(j)$ is the maximum probability among all the paths whose state is j until moment$t$; j is the possible state value at the previous moment $t-1$. In the Viterbi path search, indoor map constraints are incorporated into the state-transition evaluation. For each transition between two consecutive candidate states, the connecting segment is checked against the passable-area boundaries of the indoor map. If the transition crosses a wall or obstacle, it is treated as an infeasible transition and assigned a negligible transition score, so that it is excluded from the optimal-path competition. Transitions that remain within passable corridors and connected regions retain their normal scores. Through this constraint mechanism, the Viterbi search selects the most probable state sequence while preventing wall-crossing and obstacle-crossing trajectories.

3.3 Fusion Positioning Proposed Methodology Based on Geomagnetic Assistance and Adaptive Filtering

After the map matching constraint, the trajectory through-wall and drift problem of PDR positioning was effectively alleviated, but relying solely on inertial calculation and map correction was still difficult to deal with the cumulative deviation caused by long walking, and the position features contained in the geomagnetic signal were not fully utilized [21-22]. Geomagnetism, as a naturally stable positioning signal in the room, has the advantages of no equipment deployment and strong applicability. To fully exploit the position discrimination ability of geomagnetic sequences and improve the efficiency and accuracy of geomagnetic matching, a fast geomagnetic sequence matching method based on UCR-DTW was introduced in the study, as shown in Figure 5.

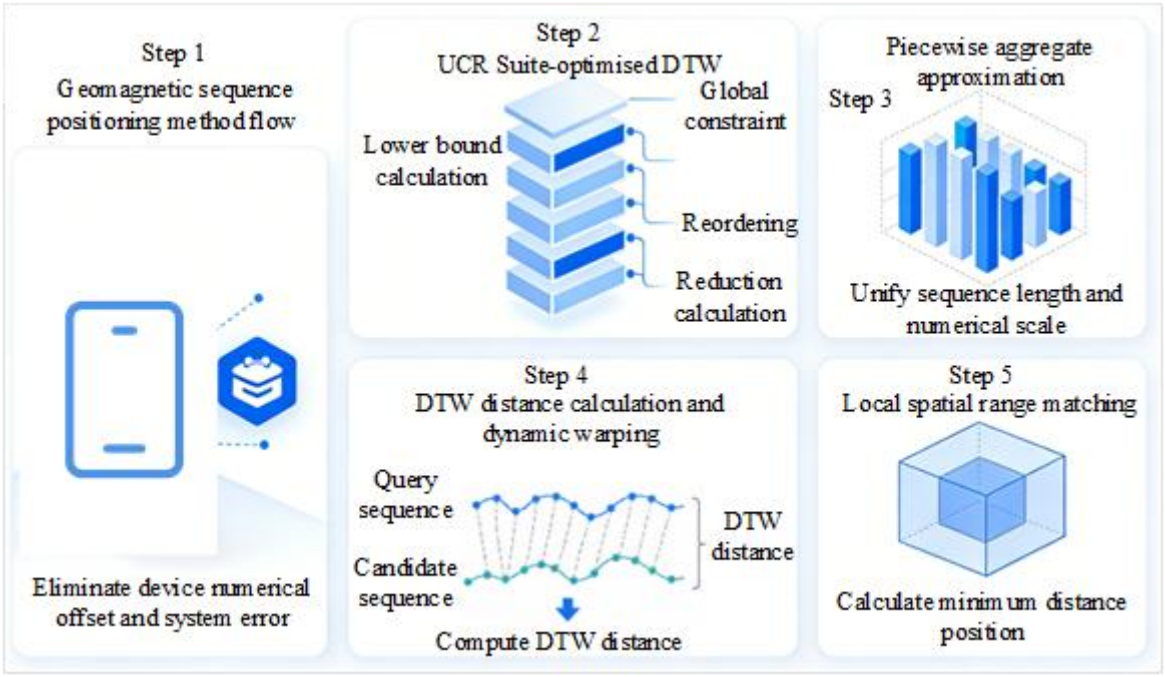

Fig. 5. Flowchart of rapid matching of geomagnetic sequences based on UCR-DTW

According to Figure 5, the geomagnetic sequences collected in real time are first subjected to standardized preprocessing to eliminate numerical offsets and system errors caused by different mobile devices. The UCR Suite optimization techniques are then integrated into the DTW algorithm to improve geomagnetic sequence matching efficiency. Global constraints are applied to restrict the warping path, and the lower-bound distance is calculated to pre-screen candidate sequences with low similarity. The UCR-DTW lower bound distanceLB calculation is shown in Equation (9).

$$LB = max(|first(M) - first(J)|, |last(M) - last(J)|) \tag{9}$$

In Equation (9), $first(M)$ represents the first element of the sequence M; $last(M)$ represents the last element of the sequence M; $first(J)$ represent the first element of the candidate sequence$J$; $last(J)$ represents the last element of the candidate sequence$J$. Candidate sequences whose lower-bound values exceed the current matching criterion are discarded without performing the full DTW distance calculation. Therefore, unnecessary dynamic-programming operations can be avoided, and complete DTW matching is performed only for the retained candidates. Sequence reordering and cascading lower-bound screening are further used to improve pruning efficiency. For the remaining geomagnetic sequences, piecewise aggregation is applied to unify sequence length and scale before the full DTW distance is calculated. The matching process is limited to the local space of the map, traversing all geomagnetic fingerprint sequences in that area, calculating the regular distance between the real-time sequence and the candidate sequence, and taking the position corresponding to the minimum distance.

To fully integrate the advantages of fast geomagnetic sequence matching and PDR location sources and offset their respective errors, an integrated positioning framework combining adaptive filtering and CRFs is studied to achieve continuous, stable, and high-precision indoor location solutions. The fusion positioning proposed methodology based on the combination of Sage-Husa adaptive Kalman filtering and improved CRFs is shown in Figure 6.

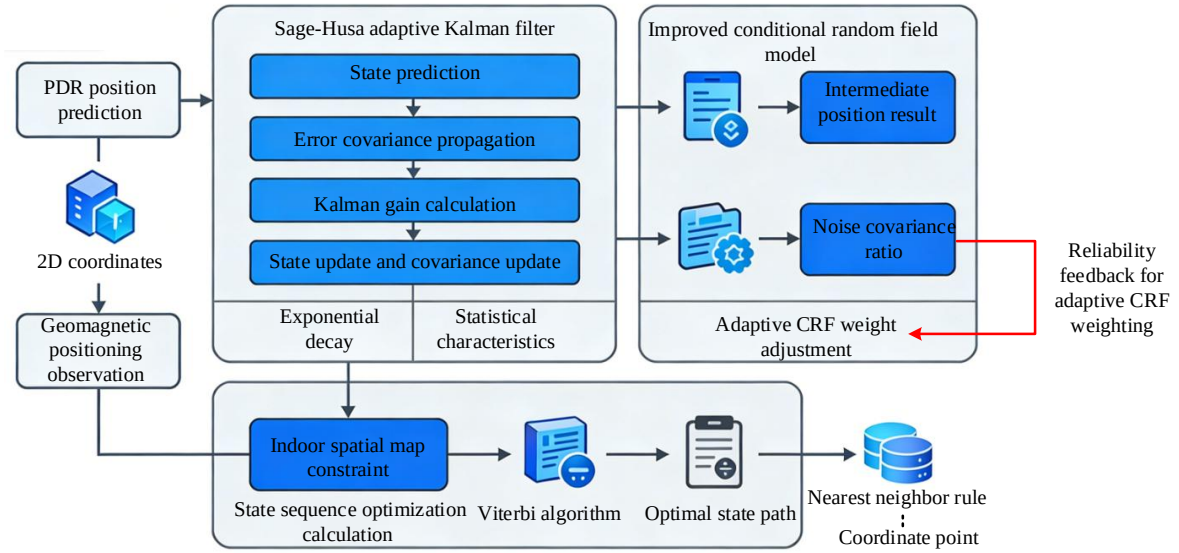

Fig. 6 Schematic diagram of PDR and geomagnetic field fusion

As shown in Figure 6, the PDR position prediction equation and the geomagnetic positioning observation equation are first established, and the two-dimensional planar coordinates are taken as the system state variables and input into the Sage-Husa adaptive Kalman filter. During filtering, state prediction, error covariance propagation, Kalman gain calculation, state update, and covariance update are performed sequentially. To adapt to the dynamic variations in PDR accumulated error and geomagnetic observation noise, the innovation sequence is used to estimate the process noise covariance matrix and the observation noise covariance matrix online. The innovation vector at time k is expressed as shown in Equation (10).

$$e_k = z_k - H_k \hat{x}_{k|k-1} \tag{10}$$

In Equation (10), where e_k denotes the innovation vector at time k, z_k denotes the position observation obtained from geomagnetic sequence matching; H_k denotes the observation matrix; and $\hat{x}_{k|k-1}$ denotes the prior predicted state calculated by PDR. The innovation vector reflects the deviation between the current geomagnetic observation position and the PDR-predicted position, and its variation can be used to characterize the dynamic behavior of observation noise and prediction error. To reduce the influence of earlier noise statistics on the current filtering result, an exponential decay factor b is introduced, and an adaptive weight varying with the iteration index is constructed. In this study, b =0.98, and the corresponding adaptive weight is expressed as shown in Equation (11).

$$d_k = \frac{1-b}{1-b^{k+1}} \tag{11}$$

In Equation (11), d_k denotes the adaptive weight at time k; b denotes the exponential decay factor; and k denotes the current filtering instant. As the filtering process proceeds, d_k weights the historical noise statistics according to the decay factor, thereby giving more effective emphasis to recent observations in covariance estimation. After obtaining the innovation vector and adaptive weight, the geomagnetic positioning observation noise is recursively estimated. The observation noise covariance matrix Rk is updated as shown in Equation (12).

$$R_k = (1 - d_k)R_{k-1} + d_k\left(e_k e_k^T - H_k P_{k|k-1} H_k^T\right) \tag{12}$$

In Equation (12), R_k and R_{k-1} denote the observation noise covariance matrices at the current and previous instants, respectively; $P_{k|k-1}$ denotes the state prediction error covariance matrix; and the superscript T denotes matrix transposition. By jointly correcting R_k using the innovation term and the prediction error covariance, the reliability of the geomagnetic observation in fusion positioning can be dynamically adjusted according to the geomagnetic matching quality.

Meanwhile, to characterize the variation in the PDR state prediction error during motion, the process noise covariance matrix is adaptively updated, as shown in Equation (13).

$$Q_k = (1 - d_k)Q_{k-1} + d_k\left[K_k e_k e_k^T K_k^T + P_{k|k} - F_k P_{k-1|k-1} F_k^T\right] \tag{13}$$

In Equation (13), Q_k and Q_{k-1} denote the process noise covariance matrices at the current and previous instants, respectively; K_k denotes the Kalman gain matrix; $P_{k|k}$ denotes the error covariance matrix after state updating; $P_{k-1|k-1}$ denotes the posterior error covariance matrix at the previous instant; and F_k denotes the state transition matrix. Through the synchronous recursive updating of Q_k and R_k, the filter can dynamically adjust the weights of PDR prediction and geomagnetic observation according to their respective error levels, thereby reducing the estimation bias caused by fixed noise parameters in complex indoor environments.

Subsequently, the intermediate position result and noise covariance information obtained from the Sage-Husa filter are input into the conditional random field model. The weights of the state feature functions are dynamically adjusted according to the reliability of different positioning information. Combined with indoor map constraints, the Viterbi algorithm is then used to search for the optimal state path, and the fused position is finally matched to the corresponding indoor map coordinates using the nearest-neighbor rule. The complete feedback fusion process is shown in Algorithm 1.

Algorithm 1. Feedback fusion of Sage-Husa filtering and improved CRF

Input: PDR predicted position, geomagnetic matching position, indoor map

Output: Final map-constrained position

1: Initialize the Sage-Husa filter, noise covariance matrices, and CRF parameters
2: For each positioning instant k:
3: Obtain the PDR prior predicted position
4: Obtain the geomagnetic matching observation
5: Calculate the innovation vector according to Equation (10)
6: Calculate the adaptive weight according to Equation (11)
7: Recursively update the observation noise covariance matrix according to Equation (12)
8: Recursively update the process noise covariance matrix according to Equation (13)
9: Perform the Sage-Husa state update and obtain the intermediate position estimate
10: Evaluate the relative reliability of the PDR prediction and geomagnetic observation according to the updated covariance information
11: Update the CRF candidate state set using the intermediate position estimate
12: Dynamically adjust the corresponding CRF state-feature weights according to reliability
13: Apply indoor map constraints and remove infeasible state transitions
14: Perform Viterbi search to determine the optimal feasible state path
15: Map the selected state to the corresponding indoor coordinate using the nearest-neighbor rule
16: End For

4. Results

4.1 Motion State Recognition and Geomagnetic Matching Performance Testing

This study employed the smartphone-based indoor positioning dataset from Track 3 of the IPIN 2025 competition for algorithm validation. The dataset was collected and released by the IPIN 2025 organizing committee in a real multi-story university building in Tampere, Finland. It contains multimodal data, including WiFi, BLE, geomagnetic field, inertial sensors, barometer, light sensor, audio, and GNSS data, together with training, testing, and scoring data, indoor maps, and evaluation tools. To reduce the influence of different smartphone carrying modes, sensor attitudes, and high-frequency motion disturbances on pedestrian positioning, the accelerometer, gyroscope, and magnetometer data were first synchronized, resampled, and low-pass filtered. Features related to displacement, heading variation, and spatial geomagnetic distribution were then extracted for PDR step detection, heading estimation, and geomagnetic matching. Unified preprocessing and feature normalization were applied to improve the consistency of multi-sensor features, and the experiments focused on evaluating trajectory drift suppression, map matching, and fusion positioning accuracy. In the experiments, the sampling frequencies of the accelerometer, gyroscope, and magnetometer were uniformly set to 100 Hz. The multi-sensor data were synchronized based on timestamps and resampled using linear interpolation. Accordingly, the time interval between adjacent samples was 0.01 s, and a sliding window of 32 samples corresponded to a local sensor sequence of 0.32 s. The peak detection threshold was set to 0.6g, the lower-bound constraint radius for geomagnetic matching was set to 6, the initial covariance of the Sage-Husa filter was set to 0.01, the feature weight of the improved CRF was set to 0.7, and the maximum number of iterations was set to 6. The study set up a simulation test platform and conducted experiments on the Ubuntu 22.04 LTS operating system. The specific configuration of the experimental environment is shown in Table 1.

Table 1. Detailed information of the testing platform

-	Configure	Parameter
Hardware configuration	CPU	Intel Core i9-14900K
	Storage	1TB NVMe SSD+2TB HDD
Software configuration	Operating system	Ubuntu 22.04 LTS
	Numerical calculation library	NumPy 1.26.0
	Data processing tool	NetworkX 2.8.8
	Containerization tool	Docker 26.1.3

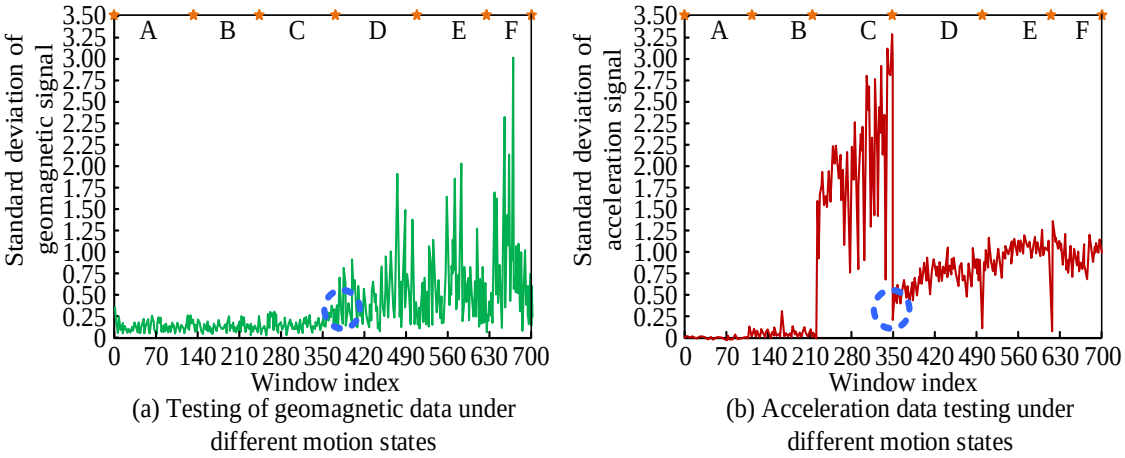

(a) Testing of geomagnetic data under different motion states

(b) Acceleration data testing under different motion states

Fig. 7. Tests of geomagnetic standard deviation and acceleration standard deviation under different motion states

To ensure the reliability and statistical significance of the experimental results, all experiments were independently repeated five times, the average was taken as the final result, and the standard

deviation was calculated to measure the range of fluctuations. The experiment explored the effectiveness and limitations of the standard deviation of the geomagnetic signal and the standard deviation of the acceleration signal in differentiating the pedestrian in stationary, slightly wobbling, general wobbling, slow walking, normal walking, and fast walking (indicated by A, B, C, D, E, F, respectively) states. The experiment collected data from multiple sets of samples, calculated the standard deviation within the sliding window in each state, and compared the separation of the two types of signals between non-motion and motion states. The test results are shown in Figure 7.

As shown in Figure 7 (A), the geomagnetic standard deviations of the non-motion states (A, B, C) were all below 0.3, and the median and interquartile range of the three almost coincide; The standard deviations of the motion states (D, E, F) were all above 0.3 and showed an upward trend with the increase of step speed. The reason was that the position of the equipment was fixed or only slightly moving when it was not in motion, and the magnetic field environment was stable; When moving across different spaces and experiencing magnetic field variations, geomagnetic fluctuations increased. As shown in Figure 7(b), the standard deviations of acceleration remain relatively low under the stationary and slight-jolt states, whereas the value under the general-jolt state C increases markedly and partially overlaps with those of slow walking D and normal walking E. This overlap indicates that relying solely on acceleration features may cause local severe jolts to be misclassified as actual walking states, thereby affecting subsequent gait detection and PDR trajectory estimation. As shown in Figure 7(a), the geomagnetic standard deviation under state C remains below 0.3, while those under the walking states D, E, and F are all above 0.3. Using 0.3 as the secondary discrimination threshold, state C and the walking states are completely separated in the tested samples, corresponding to a separation rate of 100%. Therefore, when acceleration features cannot clearly distinguish the motion state, the geomagnetic standard deviation is introduced for second-level judgment, thereby reducing the ambiguity caused by overlapping acceleration features.

The experiment aimed to evaluate the positioning accuracy and stability of the geomagnetic sequence matching algorithm based on UCR-DTW in different indoor environments. Twenty test sequences of approximately 2.4 m in length were collected in each area, including Zone 1 (strong magnetic interference area), Zone 2 (conventional corridor area), and glass corridor area (weak magnetic interference area) on the third floor of the School of Environmental Measurement. Positioning was carried out using the research proposed methodology and the fastDTW algorithm, with positioning error as the indicator. The test results are shown in Figure 8.

As shown in Figure 8 (a), the probability of the research proposed methodology having a positioning error of less than 2 m in one area was approximately 45%, and the probability of less than 5 m was approximately 75%, while the fastDTW algorithm was slightly worse. Due to the presence of electronic lockers, computers, and other equipment in Zone 1, the magnetic field gradient changed sharply, and multiple similar waveforms were prone to occur within the short sequence, making it difficult for DTW matching to uniquely determine the position, resulting in an overall large positioning error. As shown in Figure 8 (b), the probability of the research proposed methodology having a positioning error of less than 2 m in Zone 2 was approximately 60%, and the probability of less than 5 m was more than 85%. The positioning performance was superior to that of Zone 1. Since Zone 2 was a common corridor, the magnetic field variation was mainly caused by the building structure, the variation pattern was monotonous, and the short sequence feature was unique. Therefore, the matching accuracy was high and the distribution of positioning errors was more concentrated. Figure 8 (c) indicates that the probability of the positioning error of the study proposed methodology being less than 1m was approximately 40%, and the probability of being less than 2 m was more than 75%. The positioning accuracy was significantly better than that of Zone 1 and Zone 2. Due to the less ferromagnetic interference in the glass corridor area, the geomagnetic signal was derived from natural variations, the noise was low and the similarity of short sequences was low, so the probability of mismatching was minimal.

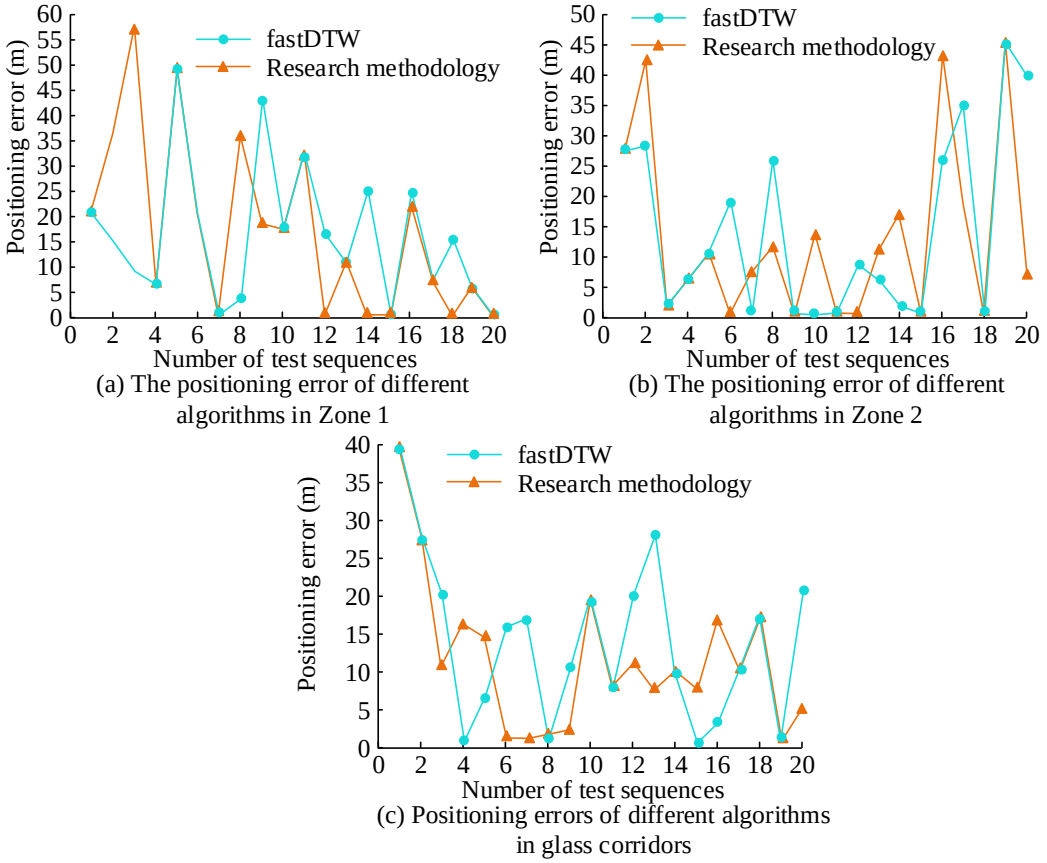

Fig. 8. Positioning error test of geomagnetic matching algorithm in different indoor areas

4.2 Verification of Accuracy and Real-Time Performance of Fusion Positioning Algorithm

The experiment was conducted to verify the advantages of the integrated fusion positioning framework combining Sage-Husa adaptive Kalman filter with improved CRFs in terms of accuracy and real-time performance by comparing two benchmarks proposed methodologies: traditional Kalman +CRFs and only improved CRFs. On the IPIN 2025 indoor positioning dataset, positioning errors were counted along eight consecutive path points, and the time spent on a single positioning was tested during the 15 s – 31 s consecutive positioning period to evaluate the accuracy and real-time performance of the algorithm. The test results are shown in Figure 9.

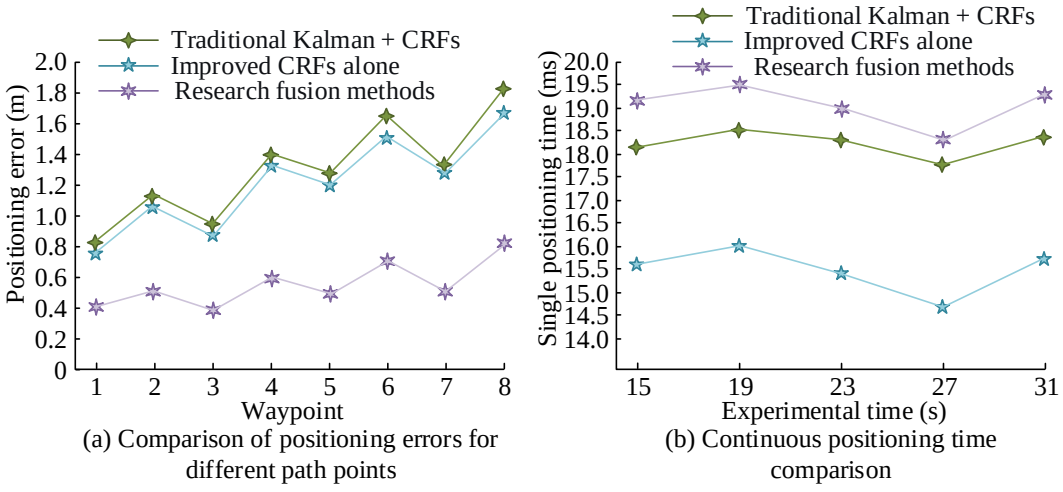

Fig. 9. Positioning accuracy and real-time test of adaptive filtering and improved CRF fusion

As shown in Figure 9 (a), with the advancement of path points, the positioning errors of all three proposed methodologies showed a slight upward trend. The error of the research fusion proposed methodology was always the lowest, with an average error of approximately 0.53 m for the 8 path points, which was about 58.2% lower than the traditional Kalman + CRFs and about 47.6% lower than the improved CRFs alone. The reason was that the Sage-Husa adaptive filter dynamically corrected noise and suppressed inertial cumulative error, while the improved CRFs provided spatial constraints on the map, and they complemented each other. The mean positioning error of 0.53 m reported here corresponds specifically to the eight consecutive path points used in Figure 9, whereas the overall mean error of 0.45 m in Table 2 is obtained from the complete fusion-positioning evaluation. As shown in Figure 9 (b), the time consumption of the three proposed methodologies remained stable in 15 s - 31 s continuous positioning. The single time consumption of the study fusion proposed methodology was between 18.3ms and 19.5 ms, slightly higher than the other two proposed methodologies, but the overall fluctuation was less than 1.2 ms, and the real-time performance met the indoor positioning requirements. The reason was that the fusion proposed methodology added adaptive filtering and multi-source fusion, but used lightweight feature extraction and Viterbi optimization, which was less costly. In addition, the state-update latency after a velocity change is mainly determined by the motion-state recognition window and the computation time of the fusion positioning process. The sampling frequency is 100 Hz and the sliding-window length is 32 samples; therefore, one complete local sequence corresponds to 0.32 s. When the motion state switches among slow, normal, and fast speeds, the DTW module updates the sliding window to re-identify the current motion state and simultaneously adjusts the peak-detection parameters. Under full-window updating, the algorithmic response time to a state change is approximately 0.32 s. With an additional fusion-positioning computation time of approximately 19.1 ms per update, the total response latency remains within approximately 0.34 s. This analysis indicates that the proposed method can complete velocity-state updating and position correction within a sub-second time scale.

The necessity and contribution of the core modules of PDR, geomagnetic matching, improved CRFs, and Sage-Husa adaptive filtering were verified through ablation experiments. Five sets of comparisons were set up, with key modules retained/added in sequence as indicators of average positioning error, maximum drift distance, positioning real-time performance, and trajectory integrity rate. The test results are shown in Table 2.

Table 2. Comprehensive test of ablation experiment

Test type	Average positioning error (m)	Maximum drift distance (m)	Positioning real-time (ms)	Trajectory integrity rate (%)
Basic PDR	2.75	5.82	12.60	62.40
PDR + Geomagnetic Matching	1.85	4.13	14.30	71.80
PDR + Improved CRFs	1.11	2.06	16.80	89.30
PDR + SAGE-Husa Filtering	0.94	1.75	15.50	86.70
Proposed Fusion proposed methodology	0.45	0.81	19.10	98.20

As shown in Table 2, performance improved step by step from the basic PDR to the full fusion proposed methodology. The average error of the base PDR was 2.75 m, the maximum drift was 5.82 m, and the trajectory completeness rate was only 62.4%. With the addition of geomagnetic matching, the average error was reduced to 1.85 m and the completeness rate was 71.8%; With the addition of the improved CRFs, the average error was 1.11 m and the integrity rate was 89.3%; The average error was 0.94 m after adding Sage-Husa filtering. The study complete proposed methodology fused all modules, with an average error of only 0.45 m, a maximum drift of 0.81 m, a trajectory completeness rate of 98.2%, and real-time performance of 19.1 ms, meeting the requirements of high-precision positioning. Geomagnetic assistance for position features, improved CRFs for spatial constraints, and Sage-Husa filtering to suppress cumulative errors - all three were indispensable.

4.3 Improved CRFs Map Matching Convergence and Anti-Interference Analysis

To verify the performance of the improved CRFs map matching proposed methodology in terms of convergence speed and anti-interference ability, the matching convergence performance was tested by different iterations, the robustness was tested under interference intensity levels 1 to 5, and the matching accuracy rate, effective constraint rate, and spatial compliance rate were statistically analyzed. Levels 1-5 corresponded to 5, 10, 15, 20, and 25 μT, respectively. The test results are shown in Figure 10.

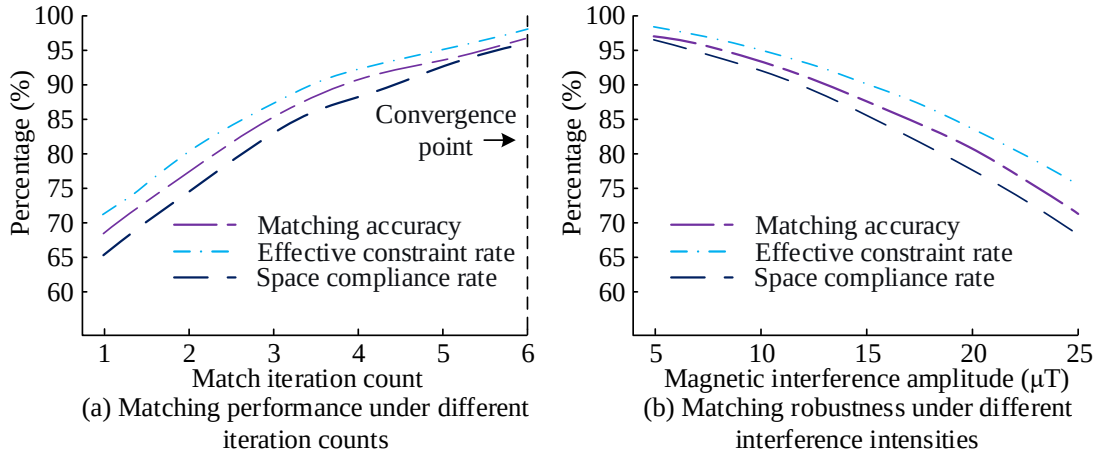

Fig. 10. Improved CRF map matching convergence and anti-interference performance test

From Figure 10 (a), with the increase of the number of iterations, the matching accuracy rate, the effective constraint rate and the spatial compliance rate continued to rise and converged rapidly, reaching 96.8%, 97.9% and 95.7% respectively after 6 iterations. The convergence curves become progressively flatter near the sixth iteration, indicating that further iterations would provide only limited accuracy improvement while increasing computational cost. Therefore, six iterations were adopted as a practical compromise between matching performance and processing efficiency. The reason was that the improved CRFs optimized the feature function and weight adaptation, quickly integrated geomagnetic and topological constraints, and eliminated invalid points one by one, allowing the map constraints to be fully exerted. As shown in Figure 10 (b), the three indicators gradually decreased as the interference level increased, but the improved CRFs decreased gently, maintaining a matching accuracy rate of 71.6% and a spatial compliance rate of 68.4% under level 5 strong interference. The reason was that the proposed methodology introduced tolerance constraints and local space limitations to reduce the influence of magnetic interference and noise; High trajectory compliance and matching accuracy are maintained in strong interference environments by weighting adaptive enhancement of reliable features and weakening of anomaly observations.

5. Conclusion

In response to the practical problems of satellite signal unavailability, complex magnetic interference, severe inertial positioning drift, and trajectories crossing walls or boundaries in smart buildings, this study focused on improving the positioning accuracy, robustness, and real-time performance of indoor pedestrian positioning and constructed an integrated positioning system combining adaptive PDR, geomagnetic matching, and map constraints. The system uses acceleration and geomagnetic dual features to identify motion states, applies DTW-based adaptive gait detection and robust adaptive Kalman filtering to improve the reliability of PDR estimation, and incorporates spatial topological constraints through an improved CRF combined with UCR-DTW for efficient geomagnetic sequence matching. The estimated trajectory is further corrected to the indoor map through the joint optimization of Sage-Husa adaptive filtering and the improved CRF. Experimental results showed that the complete fusion method achieved a mean positioning error of 0.45 m, a maximum drift of 0.81 m, a trajectory integrity rate of 98.2%, and a single-

positioning time of less than 20 ms. The improved CRF achieved a matching accuracy of 96.8% after six iterations and maintained a matching accuracy of 71.6% under strong magnetic interference of 25 μT. These results demonstrate the practical potential of the proposed method for continuous pedestrian positioning and location-assisted services in smart buildings. However, the method still shows limited stability in areas with dense strong magnetic interference and during short-sequence geomagnetic matching, and height information has not yet been fully integrated for multi-floor transitions. Future work will further investigate multi-floor topological constraints, height information, and multimodal sensing fusion to improve robustness in complex environments and cross-floor positioning performance.

References

[1] Sharma S, Kumar N, Kaur M. Conventional system to deep learning based indoor positioning system. Indian Journal of Engineering and Materials Sciences, 2024, 31 (1): 7-24. https://doi.org/10.56042/ijemsv31i1.5183

[2] Zhong C M, Lin R H, Zhu H L, Lin Y H, Zheng X, Zhu L H, et al. UWB-based AOA indoor position-tracking system and data processing algorithm. IEEE Sensors Journal, 2024, 24(19): 30522-30529. https://doi.org/10.1109 /JSEN.2024.3442192

[3] Wei Z, Chen J, Tang H, Zhang H. RSSI-based location fingerprint proposed methodology for RFID indoor positioning: A review, Nondestructive Testing and Evaluation, 2024, 39 (SI1) : 3-31. https://doi.org/10.1080/10589759.2023.2253493

[4] Rana L, Park J G. An enhanced indoor positioning proposed methodology based on RTT and RSS measurements under LOS/NLOS environment. IEEE Sensors Journal, 2024, 24 (19) : 31417-31430. https://doi.org/10.1109/JSEN.2024.3441247

[5] Li L, Zhao D, Xia Y. Indoor positioning systems based on a modified matrix-weighted fusion estimator with multipath and NLOS Mitigation. IEEE Internet of Things Journal, 2024, 11 (24) : 40041-40050. https://doi.org/10.1109/JIOT.2024.3450319

[6] Rakthanmanon T, Campana B, Mueen A, Batista G, Westover B, Zhu Q, Zakaria J, Keogh E. Searching and mining trillions of time series subsequences under dynamic time warping. Proceedings of the 18th ACM SIGKDD International Conference on Knowledge Discovery and Data Mining, 2012: 262-270. https://doi.org/10.1145/2339530.2339576

[7] Giao B C, Anh D T. Similarity search for numerous patterns over multiple time series streams under dynamic time warping which supports data normalization. Vietnam Journal of Computer Science, 2016, 3(3): 181–196. https://doi.org/10.1007/s40595-016-0062-4

[8] Han Y, Li Z, Zhao Z, Braun T. CrowdBERT: crowdsourcing indoor positioning via semi-supervised BERT with masking. IEEE Internet of Things Journal, 2024, 11(24): 40100-40112 https://doi.org/10.1109/JIOT.2024.3450710

[9] Pinto B, Oliveira H. Online RSSI selection strategy for indoor positioning in low-effort training scenarios. Computing, 2024, 106(6): 2059-2077. https://doi.org/10.1007/s00607-024-01285-y

[10] Nguyen D K, Duong T H, Nguyen L C, Hoang M K. Performance enhancement of Wi-Fi fingerprinting-based indoor positioning using truncated singular value decomposition and LSTM model. International Journal of Advanced Computer Science and Applications, 2024, 15(5): 281-288 https://doi.org/10.14569 /IJACSA. 2024.0150529

[11] Yang Y, Yang Q, Zhang T, Huang W. A Brownian motion restricted K-nearest neighbor algorithm for indoor positioning. Wireless Personal Communications, 2024, 139(1): 625-651. https://doi.org/10.1007/s11277-024-11640-z

[12] Assayag Y, Oliveira H, Souto E, Barreto R, Pazzi R. A model-based BLE indoor positioning system using particle swarm optimization. IEEE Sensors Journal, 2024, 24 (5) : 6898-6908. https://doi.org/10.1109/JSEN. 2024.3352535

[13] Xu Z, Wu J, Liu Q. Research on mobile robot indoor positioning mapping based on front-end and back-end optimization. Journal of Mechanical Science and Technology, 2024, 38(5): 2555-2561. https://doi.org/10.1007/s12206-024-0434-0

[14] Liu J, Zhang L, Xu J, Shi J. Dynamic feasible region-based IMU/UWB fusion proposed methodology for indoor positioning. IEEE Sensors Journal, 2024, 24(13): 21447-21457 https://doi.org/10.1109/JSEN. 2024.3398789

[15] Wan R, Chen Y, Song S, Wang Z. CSI-based MIMO indoor positioning using attention-aided deep learning. IEEE Communications Letters, 2024, 28 (1) : 53-57, https://doi.org/10.1109/LCOMM. 2023.3335408

[16] Kim J W, Jang H J, Hwang D H, Park C. A step, stride and heading determination for the pedestrian navigation system. Journal of Global Positioning Systems, 2004, 3(1-2): 273-279. https://doi.org/10.5081/jgps.3.1.273

[17] Alvarez D, Gonzalez R C, Lopez A, Alvarez J C. Comparison of step length estimators from wearable accelerometer devices. Annual International Conference of the IEEE Engineering in Medicine and Biology Society, 2006, 2006: 5964-5967. https://doi.org/10.1109/IEMBS.2006.259593
[18] Xu H, Meng F, Liu H, Shao H, Sun L. An adaptive multisource data fusion indoor positioning proposed methodology based on collaborative Wi-Fi fingerprinting and PDR Techniques. IEEE Sensors Journal, 2024, 24 (19) : 31481-31494. https://doi.org/10.1109/JSEN.2024.3443096
[19] Pu Q, Lan X, Zhou M, Jiang F, Cai R, Guo L. RIS-aided indoor positioning system based on passive reflective elements optimization. IEEE Transactions on Vehicular Technology, 2024, 73 (11) : 17095-17105. https://doi.org/10.1109/TVT.2024.3425466
[20] Wu Q, Li Z, Shao K. Location accuracy indicator enhanced proposed methodology based on MFM/PDR integration using Kalman filter for indoor Positioning. IEEE Sensors Journal, 2024, 24 (4) : 4831-4840. https://doi.org/10.1109/JSEN.2023.3345957
[21] Shao K, Li Z, Guo Q, Liu Z, Wu Q, et al. Fingerprint accuracy indication geomagnetic/PDR indoor adaptive integrated positioning based on smartphones. IEEE Sensors Journal, 2023, 23(23): 29545-29558. https://doi.org/10.1109/JSEN.2023.3327414
[22] Lin Y, Yu K. An improved integrated indoor positioning algorithm based on PDR and Wi-Fi under map constraints. IEEE Sensors Journal, 2024, 24 (15) : 24096-24107. https://doi.org/10.1109/JSEN.2024.3408249